J Fluoresc (2016) 26:1637–1643
DOI 10.1007/s10895-016-1849-5

ORIGINAL ARTICLE

Synthesis and Optical Properties of Novel Red-Emitting $PbNb_2O_6$: Eu^{3+} Phosphors

Mustafa İlhan[1] · **Mete Kaan Ekmekçi**[2] · **Abdullah Demir**[3] · **Halil Demirer**[1]

Received: 26 February 2016 / Accepted: 30 May 2016 / Published online: 20 June 2016
© Springer Science+Business Media New York 2016

Abstract Undoped and $PbNb_2O_6$:Eu^{3+} ($1.0 \leq x \leq 6.0$ mol%) phosphors were synthesized at 1100 °C for 3.5 h by the conventional solid state reaction method. Synthesized $PbNb_2O_6$:Eu^{3+} phosphors were characterized by X-ray diffraction (XRD), Scanning electron microscopy (SEM), Energy dispersive spectroscopy (EDS) and Photoluminescence (PL) analyses. The PL spectra showed series of excitation peaks between 350 and 430 nm due to the 4f–4f transitions of Eu^{3+}. For 395.0 nm excitation, emission spectra of Eu^{3+} doped samples were observed at 591 nm (orange) and 614 nm (red) due to the $^5D_0 \rightarrow {}^7F_1$ transitions and $^5D_0 \rightarrow {}^7F_2$ transitions, respectively. PL analysis results also showed that the emission intensity increased by increasing Eu^{3+} ion content. No concentration quenching effect was observed. The CIE chromaticity color coordinates (x,y) of the $PbNb_2O_6$:Eu^{3+} phosphors were found to be in the red region of the chromaticity diagram.

Keywords $PbNb_2O_6$ · XRD–SEM · Eu^{3+} · Photoluminescence · Red LEDs

✉ Mustafa İlhan
mustafa.ilhan@marmara.edu.tr

[1] Department of Metallurgical and Materials Engineering, Marmara University, Göztepe Kampüsü, Kadıköy, 34722 İstanbul, Turkey

[2] Department of Chemistry, Marmara University, Göztepe Kampüsü, Kadıköy, 34722 İstanbul, Turkey

[3] Department of Mechanical Engineering, Marmara University, Göztepe Kampüsü, Kadıköy, 34722 İstanbul, Turkey

Introduction

Trivalent RE^{3+} ions having 4f–4f inner-shell transitions possess specific features such as high luminescence yield, narrow emission line, and long decay time constant. Moreover, in recent years, red emitting diodes have been attracting great attention as next generation solid state lighting sources due to the advantages of long lifetime, energy saving, high efficiency, reliability and environmentally friendly properties [1–5]. Trivalent europium is known as an efficient activator for red emmiting phosphors due to its characteristic $^5F_0 \rightarrow {}^5I_j$ (J = 0,1,2,3,4) band transitions. The emission around 590–600 nm is due to the magnetic dipole transition $^5D_0 \rightarrow {}^7F_1$ whereas the emission around 610–630 nm is due to the electric dipole transition of $^5D_0 \rightarrow {}^7F_2$, induced by the lack of inversion symmetry at the Eu^{3+} site. It can also be used in different host crystals as an efficient fluorescence activator [6–8]. Lead-based materials such as quantum dots (QDs) are important semiconductor materials due to their small direct band gap (0.41 eV) and larger excitation Bohr radius (18 nm) [9, 10]. They offer potential for various applications such as telecommunications [11, 12], tunable IR lasers and solar cells [13], NIR imaging [14], photo-detectors and photovoltaic applications [15–19].

Lead sulfide (PbS) QDs have been studied in recent years due to their structural, electrical and optical properties [20, 21]. For example, PbS QDs, with grain sizes of 10 nm emit into the near-infrared region which have been applied in the biomedical detection for cancer imaging [22], and intracellular diagnostics [23]. Small-sized PbSe has also been studied in recent years. It was reported that PbSe with a grain size of less than 8 nm emits into the near-IR [24]. Bulk PbSe has a band gap of 0.26 eV (4.7 μm) at room temperature (RT); therefore, PbSe QDs have the potential to provide PL in the mid-IR energy range (>2.5 μm) [25].

$PbNb_2O_6$ has been studied recently because of its photocatalytic [26]. dielectric and piezoelectric [27], ferroelectric [28] and thermal properties [29]. $PbNb_2O_6$ has two polymorphs: Rhombohedral, and orthorhombic. Rhombohedral is a low temperature polymorph whereas orthorhombic is a high temperature polymorph with a tungsten bronze type (TTB) structure. Metastable TTB- orthorhombic polymorph forms during rapid cooling of $PbNb_2O_6$ [30, 31]. Although rhombohedral $PbNb_2O_6$ has interesting piezoelectric properties, it has attracted little attention due to lack of research on the crystal structure and properties [32].

Various attempts have been made to synthesize $PbNb_2O_6$ such as hydrothermal synthesis [33] and formation of solid solutions [34]. A co-precipitation process in oxalic solution is used to improve the electromechanical properties of $PbNb_2O_6$ [35]. Ball milling assisted-mixed oxide synthesis [36] has also been utilized.

Several studies have been conducted to improve sintering characteristics and electrical properties by replacing some dopants for lead or niobium [37–39]. Although, $PbNb_2O_6$ has attractive dielectric, piezoelectric, ferroelectric and thermal properties no work has been reported about the photoluminescence properties of RE^{3+} doped $PbNb_2O_6$ materials so far. The solid state synthesis and photoluminescence properties of pure and Eu^{3+} doped $PbNb_2O_6$ ceramics phosphors were investigated. Microstructural and photoluminescence properties of the samples were investigated using the XRD, SEM, EDS and fluorometric analyses.

Materials and Methods

Undoped and $PbNb_2O_6$:xEu^{3+} (1.0, 3.0 and 6.0 mol%) materials were synthesized by a solid state reaction method. $Pb(NO_3)_2$ powder with purity of 99 % (Sigma-Aldrich) and Nb_2O_5 powder with purity of 99.9 % (Alfa Aesar) were used as starting materials. Eu_2O_3 powder with purity of 99.9 % (Alfa Aesar) was used as a dopant. $Pb(NO_3)_2$ and Nb_2O_5 powder mixture was prepared according to $PbNb_2O_6$ stoichiometry. Eu_2O_3 powder with various percentages was added into this mixture. These powder mixtures were homogenized in agate mortar and then sintered at 1100 °C for 3.5 h under air atmosphere in an electric furnace.

The phase compositions and crystallography parameters in sintered samples were determined by X-ray diffractometer (XRD, Rigaku Corp., D-MAX 2200) using Cu-K_α radiation at a scan rate of 2°/min between 20 and 65° and Ni filter. The morphology and elemental composition of the sintered powders were investigated by Scanning electron microscopy (SEM, JEOL Ltd., JSM-5910LV) equipped with Energy dispersive spectroscopy (EDS, OXFORD Industries INCAx-Sight 7274; 133-eV resolution 5.9 keV) after Au/Pd (gold/palladium) coating. Photoluminescence (PL) measurements, excitation and emission spectra were recorded by using a Scinco Floromaster-FS/2 model fluorometer with a Xe-arc lamp (150 W) as excitation source. All the photoluminescence measurements were performed at room temperature.

Results and Discussion

X-Ray Diffraction and SEM-EDS Analyses

Figure 1 shows the XRD patterns of undoped and doped powders. XRD pattern of $PbNb_2O_6$ samples sintered at 1100 °C for 3.5 h indicated a $PbNb_2O_6$ single phase (JCPDS card No. 29–0780) which was obtained up to 6.0 mol% Eu^{3+}. XRD analysis also revealed that $PbNb_2O_6$ samples crystallized in rhombohedral (hexagonal) symmetry with space group *R3/m* (no.160). This structure has cell parameters of a = 10.501 Å, b = 10.501 Å, c = 11.555 Å, and V = 1103 Å^3. $PbNb_2O_6$ structure could be illustrated as shown in Fig. 2 [40]. In the rhombohedral structure, based on the effective ionic radius of cations with coordination numbers (C.N.), it was assumed that, Eu^{3+} ions (r = 1.17 Å, for C.N. 6) may replace Pb^{2+} ions (r = 1.19 Å, for C.N. 6). It is obvious that Eu^{3+} ions will not be able to replace Nb^{5+} ions (r = 0.64 Å, for C.N. 6) [41]. Hence, trivalent europium ions could be located in the Pb^{2+} sites of lattice due to size effect ($r_{cation}/r_{anion} \approx 0.84$, the C.N. of Eu^{3+} is 6) and attractive ionic forces between anions and cations. Also, Fig. 3 shows a shift to higher 2 theta angles for (113) peak depending on the Eu^{3+} concentrations. Correspondingly, a decrease in lattice constant may be attributed to the

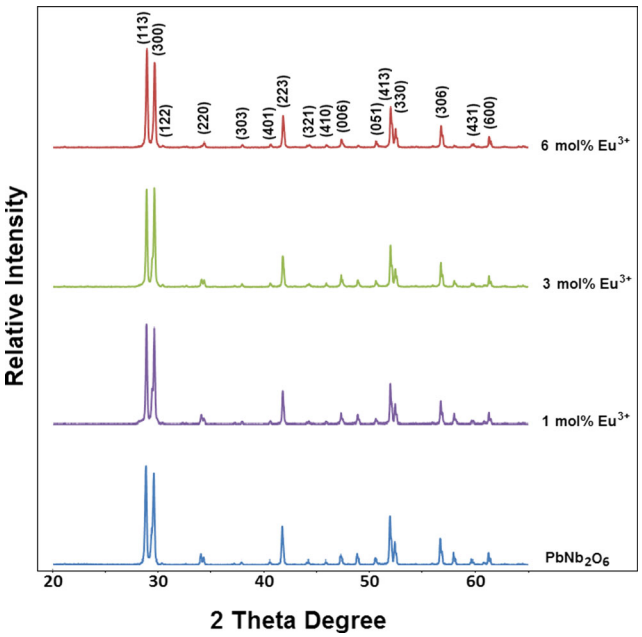

Fig. 1 X-ray diffraction patterns of undoped and Eu^{3+} doped $PbNb_2O_6$ structures between 1 to 6 mol%

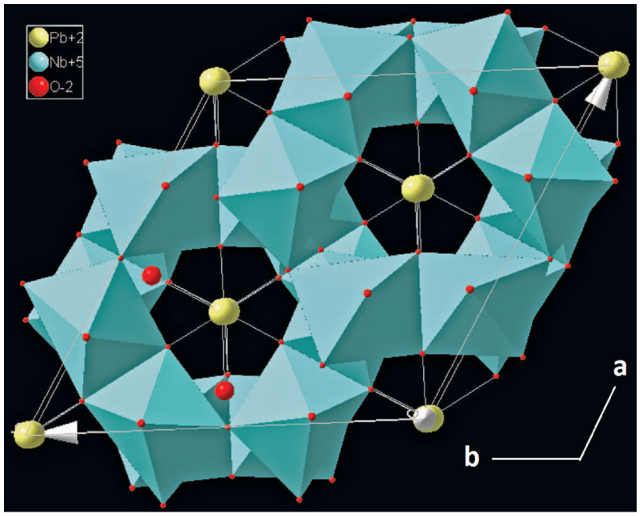

Fig. 2 Illustration of rhombohedral (hexagonal) $PbNb_2O_6$ structure

shrinkage of the lattice. These peak shifts revealed the presence of strains in the doped host lattices. This indicated the successful location of Eu^{3+} ions in the lattice up to 6.0 mol%.

SEM and EDS investigations were also in agreement with the XRD results. Figure 4(a-d) shows the SEM micrographs of undoped, 1.0, 3.0 and 6.0 mol% Eu^{3+} doped samples. SEM analysis revealed that the grain size of $PbNb_2O_6$ decreased slightly for doped samples with the increasing concentrations of Eu^{3+} ions up to 6 mol%. The structures of Eu^{3+} doped $PbNb_2O_6$ powders exhibited elongated-round and round like shapes and grain sizes varied between 0.6 and 8.0 μm. Decreases in the grain size with the increasing Eu^{3+} concentration may be attributed to the fact that the lattice distortion suppressed the abnormality of grain growth [42]. Figure 5 shows the EDS analysis which is in agreement with the theoretical and elemental composition of 6.0 mol% Eu^{3+} doped $PbNb_2O_6$ sample.

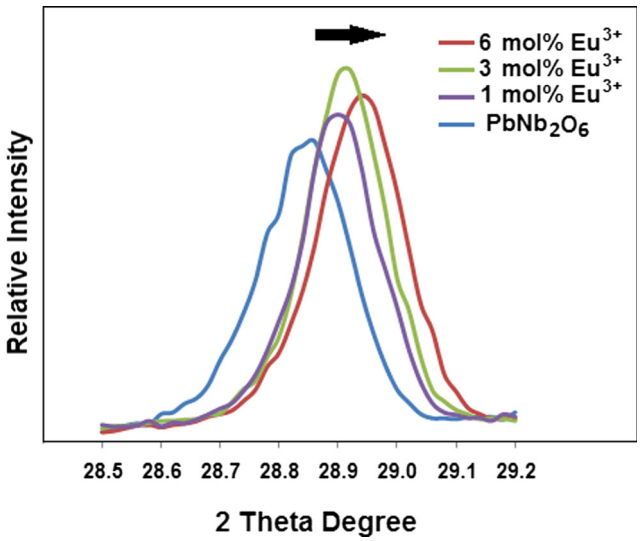

Fig. 3 Illustration of (113) peak shift to higher 2 theta angles depending on the Eu^{3+} concentrations

Based on the SEM and XRD results, it can be concluded that although the incorporation of Eu^{3+} ions did not cause change in the single phase structure of $PbNb_2O_6$ up to 6.0 mol% concentration, the incorporation of Eu^{3+} ions may affect the charge compensation in the structure.

Optical Analysis

Figure 6a shows UV–visible diffuse reflection spectrum (DRS) of $PbNb_2O_6$ which was used to obtain the host absorption spectrum (Fig. 6b) by applying the Kubelka–Munk function (1) [43]:

$$F(R) = \frac{(1-R)^2}{2R} = K/S \quad (1)$$

where R, K and S are the reflectivity, absorption, and scattering coefficients, respectively. From the absorption spectra, the optical band gap of $PbNb_2O_6$ was calculated to be about 3.28–3.33 eV by extrapolating the Kubelka–Munk function to K/S = 0. Generally, an ideal phosphor for UV-LEDs should have absorption around 365 nm or 400 nm (emission wavelengths of UV-LED chips) [44–46]. Obviously, the DRS spectrum shows strong absorption around 400 nm, indicating that it can be a candidate as a red phosphor for UV-LEDs.

Figure 7 shows the excitation spectra of $PbNb_2O_6$:xEu^{3+} (x = 1.0, 3.0 and 6.0 mol%) phosphors with emission monitored at 616 nm. The excitation spectra in the 350–430 nm range belong to the transitions between the ground level $^7F_0$ and the excited levels $^5D_4$, ^5G_J, $^5L_6$, $^5D_3$, $^5D_2$ respectively. The assignments of the different excitation bands were identified on the basis of Dieke's energy level diagram [47]. Four excitation bands were observed at $^7F_0 \rightarrow {}^5D_4$ (363 nm), $^7F_0 \rightarrow {}^5G_J$ (384 nm), $^7F_0 \rightarrow {}^5L_6$ (395 nm) and $^7F_0 \rightarrow {}^5D_3$ (416 nm). Among these excitation bands, the peak at 395 nm was used to investigate the visible photoluminescence properties of different concentrations of Eu^{3+} ions in $PbNb_2O_6$:Eu^{3+} due to sharpness and intensity of this peak.

Figure 8a shows emission spectra of $PbNb_2O_6$:xEu^{3+} (x = 1.0, 3.0 and 6.0 mol%) phosphors excited at 395 nm. Spectrofluorometric analysis of $PbNb_2O_6$:Eu^{3+} phosphors exhibited two typical emission bands at 591 nm and at 616 nm due to $^5D_0 \rightarrow {}^7F_1$ and $^5D_0 \rightarrow {}^7F_2$ transitions, respectively. The $^5D_0 \rightarrow {}^7F_1$ transition is an orange color and having the magnetic dipole transition that hardly changes the crystal field strength around the Eu^{3+} ions. When they are located in the host, this transition is also independent from the site symmetry of Eu^{3+} ions. However, the $^5D_0 \rightarrow {}^7F_2$ transition is red color and having electric dipole transition in which the site symmetry of the Eu^{3+} ions is very sensitive to the crystal field changes. The ratio of electric and magnetic dipole "($^5D_0 \rightarrow {}^7F_2$)/

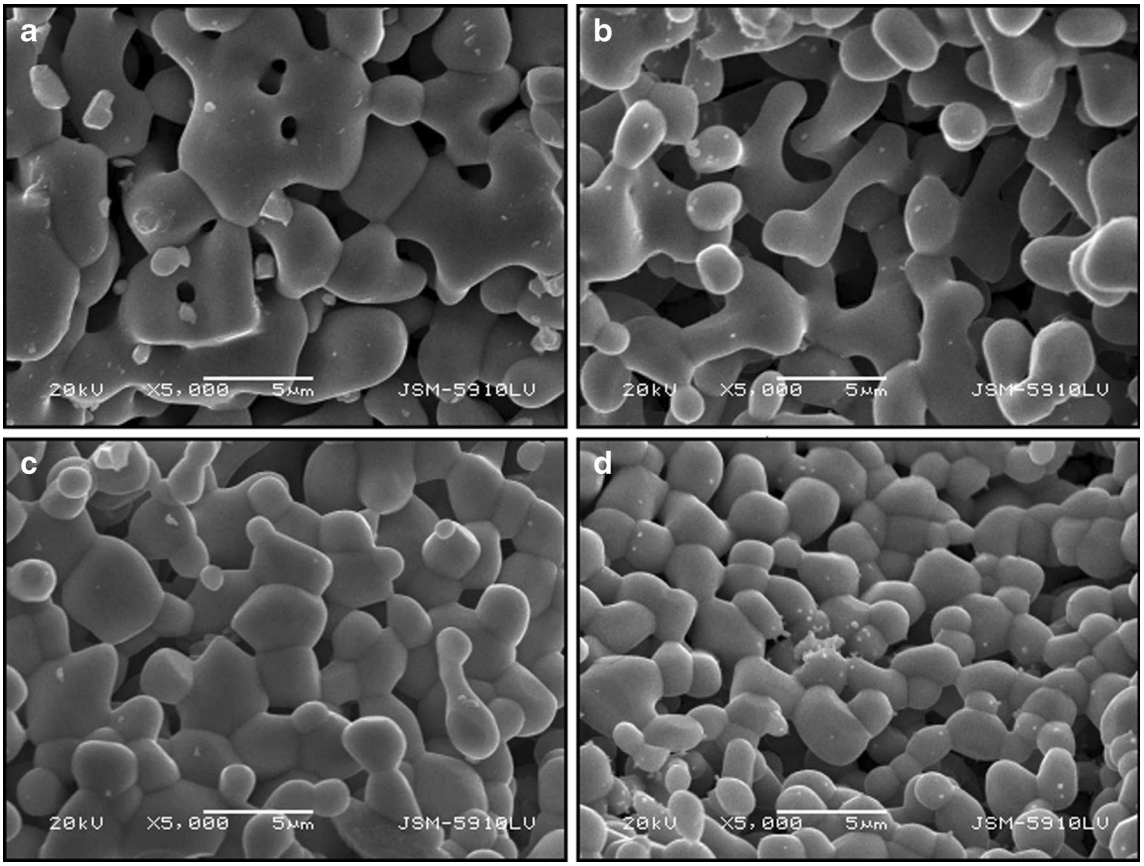

Fig. 4 SEM (seconder electron) micrographs **a** undoped and **b** 1, **c** 3, **d** 6 mol% Eu^{3+} doped $PbNb_2O_6$ structures at ×5000 magnification

($^5D_0 \rightarrow {}^7F_1$)" is indicated on the site symmetry of Eu^{3+} ions which called as the asymmetry ratio (R). As a result, $PbNb_2O_6$:xEu^{3+} phosphors indicated dominant red color depending on high asymmetry ratio.

Figure 8b shows emission spectra with respect to the variation of Eu^{3+} doping concentration. The emission intensity of Eu^{3+} ions increased with the increasing Eu^{3+} content which did not lead to the concentration quenching. While the

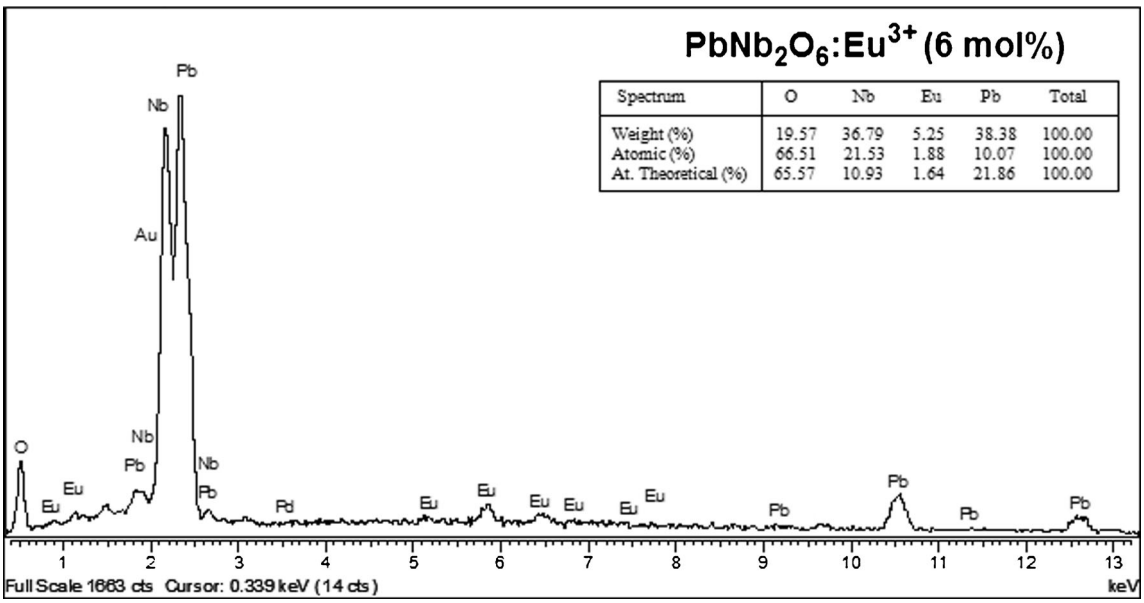

Fig. 5 Elemental analysis spectrum, weight-atomic and theoretical atomic data of Eu^{3+} doped $PbNb_2O_6$ grains at 6 mol%

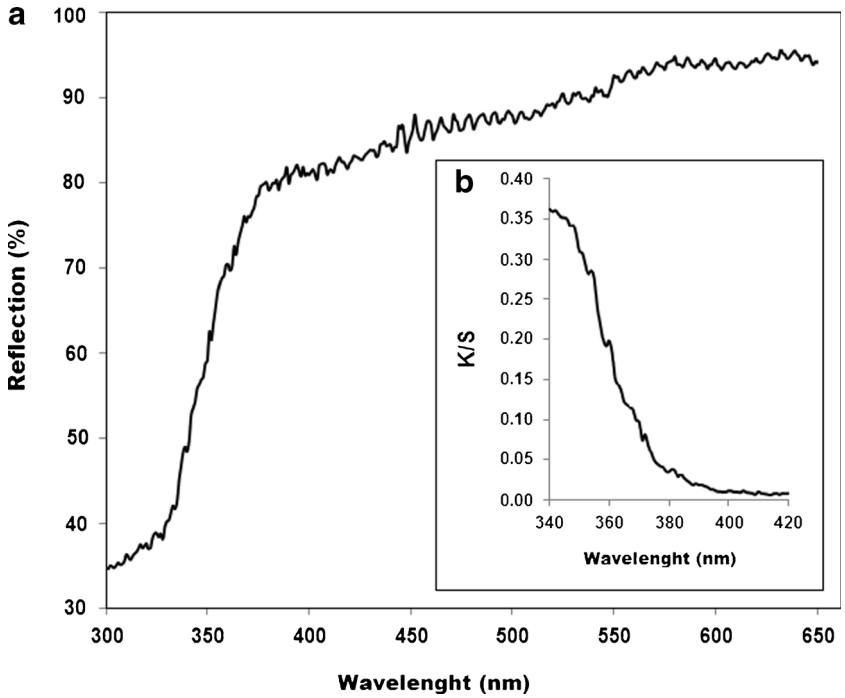

Fig. 6 **a** Diffuse reflection spectrum of $PbNb_2O_6$, **b** the absorption spectrum of $PbNb_2O_6$ obtained from the reflection spectrum by using the Kubelka-Munk function

concentration of Eu^{3+} ions increases, the distance between the Eu^{3+} ions decreases. This promotes nonradiative energy transfer between Eu^{3+} ions. Therefore, the transfer of the excitation energy strongly depends on the distance between Eu^{3+} ions. The critical distance (R_c) for energy transfer in $PbNb_2O_6$:Eu^{3+} can be estimated from by Blasse's equation (2) [48]:

$$R_c \approx 2\left(\frac{3V}{4\pi XcN}\right)^{1/3} \quad (2)$$

where the structural parameters namely unit cell volume (V), the number of available sites for the dopant in the unit cell (N) and critical concentration of dopant (X_c). The Eu^{3+} critical concentration (X_c) was 6 mol% or 0.06. For $PbNb_2O_6$:Eu^{3+} phosphor, the calculated values were as follows: $X_c = 0.06$, $V = 1103$ (Å)^3 and $N = 9$. The critical distance (R_c) was calculated as 15.74 Å. According to Blasse's theory [49, 50], when the Eu^{3+}–Eu^{3+} distance is larger than 5 Å, exchange interaction becomes ineffective.

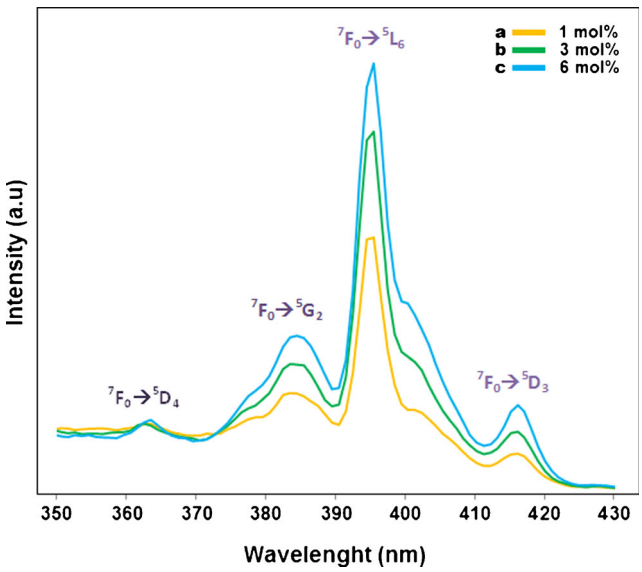

Fig. 7 Excitation spectra of $PbNb_2O_6$:Eu^{3+} phosphors monitored at 616 nm

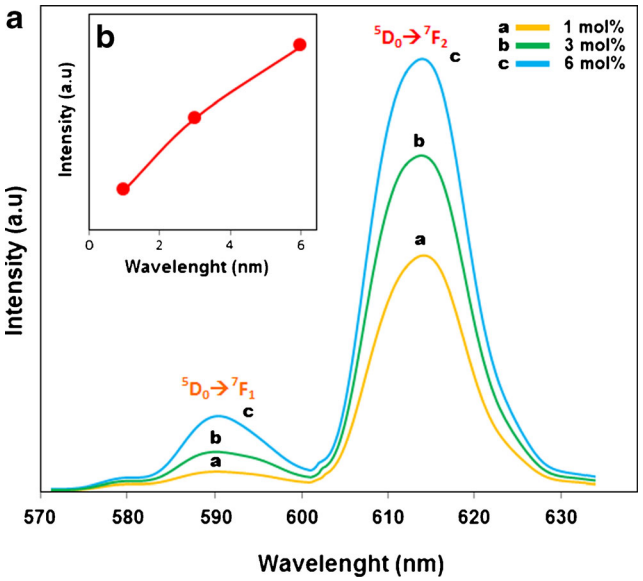

Fig. 8 **a** Emission spectra of $PbNb_2O_6$:Eu^{3+} phosphors under 395 nm excitation, **b** Emission intensities as a function of Eu^{3+} concentration at 616 nm

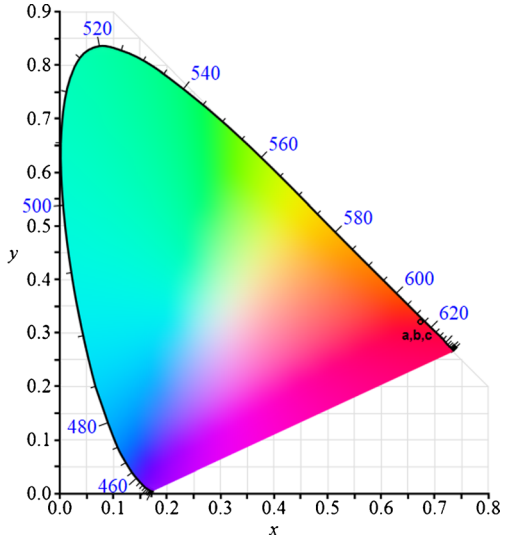

Fig. 9 The CIE chromaticity coordinate diagram of $PbNb_2O_6:Eu^{3+}$ phosphors

Figure 9 shows the Commission Internationale de I'Eclairage (CIE) chromaticity coordinates of $PbNb_2O_6:Eu^{3+}$ phosphors which were determined based on their corresponding PL spectra at 395 nm. The CIE color coordinates (x,y) were calculated as a(0.676, 0.324), b(0.671, 0.329) and c(0.667, 0.333) for 1, 3 and 6 mol% doping concentrations respectively. The value c(0.667, 0.333) was calculated to be close to the National Television Standard Committee (NTSC) values. Consequently, $PbNb_2O_6:Eu^{3+}$ phosphors having good color purity can be a good candidate as being a red LED and red emitting component of white LEDs.

Conclusions

New red-emitting Eu^{3+} doped $PbNb_2O_6$ phosphors were obtained by conventional solid state method. XRD results confirmed the presence of $PbNb_2O_6$ single phase having rhombohedral structure which formed between 1.0 and 6.0 mol% Eu^{3+} doping concentrations. SEM analysis revealed that the grains have oval shape and grain size varied from submicron to a few microns for all samples. XRD and SEM results showed that, $PbNb_2O_6:Eu^{3+}$ crystallite and grain sizes decreased depending on Eu^{3+} concentration. $PbNb_2O_6:Eu^{3+}$ phosphors exhibited an orange emission at 591 nm and a red emission at 616 nm related to ($^5D_0 \rightarrow {}^7F_1$) and ($^5D_0 \rightarrow {}^7F_2$) band pass emissions respectively. The emission intensity of Eu^{3+} ions increased with the increase of Eu^{3+} concentration. The concentration quenching phenomenon has not been observed. The CIE values were near to red light point which was x = 0.667, y = 0.333 for 6.0 mol% Eu^{3+}doped sample. Based on the results, it was concluded that the $PbNb_2O_6:Eu^{3+}$ phosphors having good color purity can be a good candidate as being a red LED and red emitting component of white LEDs.

References

1. Moura AP de, Oliveira LH de, Paris EC, Li MS, Andrés J, Varela JA, on Longo E, Rosa ILV (2011) Synthesis, structural and photophysical properties of $Gd_2O_3:Eu^{3+}$ nanostructures prepared by a microwave sintering process. J Fluoresc 21:1431–1438.
2. Vishwnath V, Srinivas M, Patel NP, Modi D, Murthy KVR (2016) Synthesis and photoluminescence studies of Eu(III), Er(III) doped strontium gadolinium tantalum oxide. J Fluoresc 26:277–282
3. Faulques E, Wery J, Dulieu B, Seybert C, Perry DL (1998) Synthesis, fabrication, and photoluminescence of CaF_2 doped with rare earth ions. J Fluoresc 8:283–287
4. Başak AS, Ekmekçi MK, Erdem M, Ilhan M, Mergen A (2016) Investigation of boron-doping effect on photoluminescence properties of $CdNb_2O_6:Eu^{3+}$ phosphors. J Fluoresc. doi:10.1007/s10895-015-1759-y
5. Yan B, Lin L, Wu J, Lei F (2011) Photoluminescence of rare earth phosphors $Na_{0.5}Gd_{0.5}WO_4:RE^{3+}$ and $Na_{0.5}Gd_{0.5}(Mo_{0.75}W_{0.25})O_4:RE^{3+}$ (RE = Eu, Sm, Dy). J Fluoresc 21:203–211
6. Wang Y, Endo T, Xie E, He D, Liu B (2004) Luminescence properties of $Ca_4GdO(BO_3)_3$:Eu in ultraviolet and vacuum ultraviolet regions. Microelectron J 35:357–361
7. Wang J, Song H, Kong X, Peng H, Sun B, Chen B, Zhang J, Xu W, Xia H (2003) Fluorescence properties of trivalent europium doped in various niobate codoped glasses. J Appl Phys 93:1482
8. Wang Z, Yuan D, Xu D, Lv M, Cheng X, Pan L, Shi X (2003) Growth and optical properties of Eu^{3+}-doped $La_3Ga_5SiO_{14}$ single crystal. J Cryst Growth 255:348–352
9. Phuruangrat A, Thongtem T, Thongtem S (2009) Preparation of ear-like, hexapod and dendritic PbS using cyclic microwave-assisted synthesis. Mater Lett 63:667–669
10. Nanda KK, Kruis FE, Fissan H, Behera SN (2004) Effective mass approximation for two extreme semiconductors: band gap of PbS and CuBr nanoparticles. J Appl Phys 95:5035–5041
11. Hoogland S, Sukhovatkin V, Howard I, Cauchi S, Levina L, Sargent EH (2006) A solution-processed 1.53 mu m quantum dot laser with temperature-invariant emission wavelength. Opt. Express 14:3273–3281
12. Moreels I, Geyter BD, Thourhout DV, Hens Z (2009) Transmission of a quantum-dot-silicon-on-insulator hybrid notch filter. J Opt Soc Am B-Opt Phys 26:1243–1247
13. Sargent EH (2005) Infrared quantum dots. Adv Mater 17:515–522
14. Kim S, Marshall AR, Kroupa DM, Miller EM, Luther JM, Jeong S, Beard MC (2015) Air-stable and efficient PbSe quantum-dot solar cells based upon ZnSe to PbSe cation-exchanged quantum dots. Am Chem Soc 9:8157–8164
15. Luther JM, Law M, Beard MC, Song Q, Reese MO, Ellingson RJ, Nozik AJ (2008) Schottky solar cells based on colloidal nanocrystal films. Nano Lett 8:3488–3492
16. McDonald SA, Konstantatos G, Zhang SG, Cyr P. W, Klem EJD, Levina L, Sargent EH (2005) Solution-processed PbS quantum dot infrared photodetectors and photovoltaics. Nat Mater 4:138–U114
17. Sargent EH (2009) Infrared photovoltaics made by solution processing. Nat Photonics 3:325–331
18. Nozik AJ (2005) Exciton multiplication and relaxation dynamics in quantum dots: applications to ultrahigh-efficiency solar photon conversion. Inorg Chem 44:6893–6899
19. Rauch T, Boberl M, Tedde SF, Furst J, Kovalenko MV, Hesser GN, Lemmer U, Heiss W, Hayden O (2009) Near-infrared imaging with quantum-dot-sensitized organic photodiodes. Nat Photonics 3:332–336
20. Hollingsworth J, Klimov V (2004) Semiconductor and metal nanocrystals: synthesis and electronic and optical properties, chapter 'Soft' Chemical Synthesis and manipulation of semiconductor nanocrystals. Marcel Dekker, Inc, New York, pp. 1–64

21. Moriarty P (2001) Nanostructured materials. P Reports on Progress in Physics 64:297
22. Hu R, Law WC, Lin G, et al. (2012) PEGylated phospholipid micelle encapsulated near-infrared PbS quantum dots for in vitro and in vivo bio-imaging. Theranostics 2:723–733
23. Fang M, Peng CW, Pang DW, Li Y (2012) Quantum dots for cancer research: current status, remaining issues, and future perspectives. Cancer Biol Med 9:151–163
24. Murray CB, Sun S, Gaschler W, Doyle H, Betley TA, Kagan CR (2001) Colloidal synthesis of nanocrystals and nanocrystal superlattices. IBM J Res Dev 45:47–55
25. Pietryga JM, Schaller RD, Werder D, Stewart MH, Klimov VI, Hollingsworth AJ (2004) Pushing the band gap envelope: mid-infrared emitting colloidal PbSe quantum dots. J Am Chem Soc 126:11752–11753
26. Xiao Q, Zhou Q, Zhang J, Ouyang L (2009) Photocatalytic decolorization of methylene blue over monoclinic pyrochlore-type $Pb_2Nb_2O_7$ under visible light irradiation. J Alloys Compd 468: L9–L12
27. Goodman G (1953) Ferroelectric properties of lead metaniobate. J Am Ceram Soc 36:368–1953
28. Soejima J, Nagata K (2001) $PbNb_2O_6$ ceramics with tungsten bronze structure for low Q_m piezoelectric material. Jpn J Appl Phys 40:5747
29. Sahu KR, De U (2009) Thermal characterization of piezoelectric and non-piezoelectric lead meta-niobate. Thermochim Acta 490: 75–77
30. Roth RS (1959) Phase equilibrium relations in the binary system lead oxide niobium pentoxide. J Res Natl Bur Stand 62:27–38
31. Francombe MH (1956) Polymorphism in lead metaniobate. Acta Crystallogr 9:683–684
32. Lopatin SS, Medvedev ES, Raevskii IP (1985) Russ J Inorg Chem 30:2102–2106
33. Lu CH, Chyi N (1996) Fabrication of fine lead metaniobate powder using hydrothermal processes. Mater Lett 29:101–105
34. Sahini MG, Grande T, Fraygola B, Biancoli A, Damjanovic D, Setter N (2014) Solid solutions of lead metaniobate-stabilization of the ferroelectric polymorph and the effect on the lattice parameters, dielectric, ferroelectric, and piezoelectric properties. J Am Ceram Soc 97:220–227
35. Yamamoto T (1991) Relations between piezoelectric properties and microstructure in poled piezoelectric ceramics by applied uniaxial compressive stress. Jpn J Appl Phys 30:2256–2259
36. Lee HS, Kimura T (1998) Effects of microstructure on the dielectric and piezoelectric properties of lead metaniobate. J Am Ceram Soc 81:3228–3236
37. Subbarao EC, Hrizo J (1962) Solid solution based on ferroelectric $PbNb_2O_6$. J Am Ceram Soc 45:528–531
38. Francombe MH (1960) The relation between structure and ferroelectricity in lead barium and barium strontium niobates. Acta Crystallogr 13:131–140
39. Chong E, Chaklader ACD, Prasad E (1992) Sintering of $PbNb_2O_6$ with dopant. Diffus Defect Data Pt B 25&26:335–342
40. Chakraborty KR, Sahu KR, De A, De U (2010) Structural characterization of orthorhombic and rhombohedral lead meta-niobate samples. Integr Ferroelectr 120:102–113
41. Speight JG (1999) Lange's handbook of chemistry, Sixteenth edn. The McGraw-Hill Companies, New York
42. Sadiq I, Khan I, Aen F, Islam MU, Rana MU (2012) Influence of rare earth Ce^{3+} on structural, electrical and magnetic properties of Sr^{2+} based W-type hexagonal ferrite. Physica B 407:1256–1261
43. Yamashita NN (1973) Luminescence centers of Ca(S: se) phosphors activated with impurity ions having s^2 configuration. I. Ca(S:se):Sb^{3+} phosphors. J Phys Soc Jpn 35:1089–1097
44. Du FP, Nakai Y, Tsuboi TJ, Huang YL, Seo HJ (2011) Luminescence properties and site occupations of Eu^{3+} ions doped in double phosphates $Ca_9R(PO_4)_7$ (R = Al, Lu). J Mater Chem 21: 4669–4678
45. Huang CH, Chen TM, Liu WR, Chiu YC, Yeh YT, Jang SM (2010) A single-phased emission-tunable phosphor $Ca_9Y(PO_4)_7$:Eu^{2+}, Mn^{2+} with efficient energy transfer for white-light-emitting diodes. ACS Appl Mater Interfaces 2:259–264
46. Zhu G, Ci Z, Xin S, Wen Y, Wang Y (2013) Warm white light generation from Dy^{3+} doped $NaSr_2Nb_5O_{15}$ for white LEDs. Mater Lett 91:304–306
47. Dieke GH (1968) Spectra and energy levels of rare earth ions in crystals. Interscience Publishers, New York
48. Blasse G (1986) Energy transfer between inequivalent Eu^{2+} ions. J Solid State Chem 62:207–211
49. Blasse G, Grabmarier BC (1994) Luminescent materials. p. 99. Springer-Verlag, Berlin.
50. Blasse G (1969) Energy transfer in oxidic phosphors. Philips Res Rep 24:131